Journal of Electronic Materials (2024) 53:4947–4955
https://doi.org/10.1007/s11664-024-11042-8

28TH INTERNATIONAL CONFERENCE ON NUCLEAR TRACKS AND RADIATION MEASUREMENTS

A Bimetallic-Doped Boron Nanosheet Electrocatalyst for Efficient Hydrogen Evolution Reaction

Akshidha Singla[1] · **Rajnish Dhiman**[2] · **Aman Mahajan**[1]

Received: 24 December 2023 / Accepted: 11 March 2024 / Published online: 9 April 2024

Abstract

Two-dimensional (2D) monometal boron nanosheets (BNS) are emerging as a promising candidate, demonstrating high catalytic performance by virtue of their tunable surface chemistry, large surface area, superb hydrophilicity, and swift charge transfer kinetics. Nonetheless, oxidation and restacking of these nanosheets in ambient air make it challenging for practical applications. The introduction of transition metals in BNSs helps to suppress interlayer restacking of the sheets. Further, the addition of bimetallic atoms help to diminish the overpotential value, correspondingly boosting the catalytic activity and onset potential required for reaction kinetics. Accordingly, herein, structural and electronic engineering of BNS using bimetallic atoms (Ag:Cu) at different doping concentrations are investigated and characterized using x-ray diffraction, Fourier transform infrared spectroscopy, field emission scanning electron microscopy, and x-ray photoelectron spectroscopy studies. Finally, the electrocatalytic performance towards hydrogen evolution reaction was investigated through cyclic voltammetry and electrochemical impedance spectroscopy to study the charge transfer rate. Here, optimized sample shows lowest overpotential value of 101 mV and Tafel slope of 59 mV dec^{-1} with highest exchange current density of 7.86 mA cm^{-2} and minimum charge transfer resistance of 15.9 Ω. Thus, current findings could help in developing the ideas for the surface modifications to significantly enhance the electrocatalytic performance.

Keywords Boron nanosheets · bimetallic doping · Ag:Cu NPs · hydrogen evolution reaction

Introduction

The increasing global energy crisis demands the production of clean and green hydrogen. As a versatile energy carrier, hydrogen holds immense potential to address various challenges associated with conventional energy systems.[1,2] The hydrogen produced by electrolysis of water through the hydrogen evolution reaction (HER) can help in meeting the global energy demands.[3] Electrolysis is basically the exchange of charge carriers between the electrode and electrolyte by splitting water into hydrogen and oxygen using some energy. The HER takes place at the cathode, where protons gain electrons to produce hydrogen gas.[4] Numerous scientific investigations have been carried out to sufficiently enhance HER performance, contributing to the advancement of a greener and environmentally friendly energy future.[5] Tang et al.[6] reported the use of multifunctional carbon based nickel nanoparticles (NC-NiNPs) as HER catalyst using polymer encapsulation which exhibited a low overpotential value of 74 mV at 10 mA cm^{-2}. For efficient catalytic activity towards HER, the electrocatalyst should have a large surface area, high conductivity, and abundant active sites.[7] Zhou et al.[8] employed the hydrogen spillover method to increase electrocatalytic activity for the HER, which helped to decrease the overpotential to 53 mV from 242 mV, respectively. Recently, Wu et al.[9] explored two-dimensional metal carbides as promising material for efficient HER studies. Inspired by this, researchers have explored various two dimensional (2D) materials for efficient electrocatalytic activity towards HER and oxygen evolution reaction (OER).[10] Liu et al.[11] reported the enhanced performance for HER using an MXene-based electrocatalyst.

✉ Aman Mahajan
aman.phy@gndu.ac.in

[1] Department of Physics, Guru Nanak Dev University, Amritsar 143005, India

[2] Department of Physics, Malaviya National Institute of Technology, Jaipur 302017, India

Among all the studied materials, the 2D allotrope of boron has gained scientific interest because of its outstanding inherent optoelectronic features.[12] 2D boron nanosheets (BNSs) are considered as an efficient material in various applications owing to their multilayered lattice structure with outstanding conductive properties.[13] They demonstrate high electrocatalytic activity, notably in the HER due to their enormous surface area, high conductivity, outstanding hydrophilicity, and rapid charge transfer kinetics.[14] Despite these multiple advantages, however, BNS are quite unstable in atmosphere because of their reactivity and sensitivity to light. They may undergo oxidation or other chemical reactions when exposed to air or moisture, limiting their stability under certain conditions.[15] Also, the interlayer restacking of these sheets makes it challenging for potential applications. Considering the aforementioned issues, various approaches have been adopted such as doping,[16] defect engineering,[17] and formation of nanocomposites,[18] to enhance their stability and catalytic activity. Introducing metal dopants into the BNSs is an efficient approach, as they act as an intercalating agent between the sheets, thereby preventing interlayer restacking and helping to enhance the catalytic performance.[19,20] Pt-group metals are widely regarded as potential dopants due to their extremely low overpotential values and nearly zero Gibbs free energy. However, their exorbitant cost and rare earth abundance limits the large-scale industrial application of H_2 production. Ag offers an option to replace conventionally used Pt-group materials for driving HER owing to its advantages of high selectivity and conductivity and large turnover frequency for H_2 generation.[21] However, HER activity using a Ag dopant alone is far from achieving Pt-like activity.[22] Moreover, in comparison to monometallic nanoparticle catalysts, bimetallic doping provides exceptional catalytic activity and stability owing to synergistic coupling effects from individual components. More importantly, an appropriate combination of binary metals is significant to achieve more effective electrocatalysis. Thus, alloying a Ag catalyst with another metal catalyst could potentially enhance its relatively inferior catalytic activity. However, like Pt, Ag does not readily combine with other metals.[21] One viable candidate to alloy with Ag and form a Ag-M composite is Cu, which has rich earth abundance and possesses several electrochemical application prospects.[23] Bimetallic Ag:Cu nanocolloids have been widely reported elsewhere and demonstrate enhanced performance; however, there is no reported literature on bimetallic Ag:Cu for electrocatalytic hydrogen production. The use of Cu with Ag provides additional active sites for H^+ ion reduction, which dramatically boosts HER activity.[24] Thus, upon introduction of the Ag:Cu bimetallic catalyst onto well-separated BNSs, the composite electrode shows improvement in HER performance relative to bare BNSs and monometallic counterparts, owing to highly active and stable Ag and Cu active sites supported on the matrix of highly conducting BNSs and strong metal-support interaction strength.

To prevent intrinsic self-restacking issues of BNSs as well as to modulate the electronic environment of active sites towards optimal binding energies, a unique combination of large-sized bimetallic transition metal (Ag:Cu) dopants were introduced into BNSs,[25,26] elucidating the role of each component in this bimetallic-doped catalyst responsible for boosted electrochemical HER performance. In the present study, a series of nanocomposites using bimetallic (Ag:Cu)-doped BNSs were synthesized by varying the weight percentages of dopants (5 wt.%, 10 wt.%, and 15 wt.%) in BNSs and their corresponding HER parameters were studied. Among them, an optimized sample with 10 wt.% of bimetallic dopants concentration showed enhanced catalytic performance by providing sufficient charge transport mechanism along with increased electrode/electrolyte interaction to pristine BNSs, which is advantageous in HER studies.

Experimental

Materials and Methods

Boron powder, polyvinylpyrrolidone (PVP, 99.9%), L-ascorbic acid ($C_6H_8O_6$), ammonium hydroxide (NH_4OH, 98 %), copper(II) chloride ($CuCl_2$, 99%), silver nitrate ($AgNO_3$, 97%), sodium borohydrate ($NaBH_4$, 98%), and Nafion 117 solution, were procured from Merck, India, and *N-N* dimethylformamide (DMF) was purchased from Spectrochem Pvt. Ltd. All the chemicals were used as received without further processing.

Synthesis of BNSs

Two-dimensional BNSs were synthesized by employing liquid exfoliation. In this process, the boron powder and DMF solution were meticulously combined in a 1:1 ratio. The samples were then subjected to probe sonication for 4 h at 225 W, with an ultrasonication probe alternating on for 2 s and off for 4 s, respectively. Subsequently, the resulting solution was then centrifuged and decanted in three to four cycles, each at varying speeds of 7000 rpm, 10,000 rpm, and 12,000 rpm with DI water to obtain residual brown colored slurry, which was then left to dry in an oven at 80°C, to yield the desired two-dimensional BNSs.

Synthesis of Ag and Cu Nanoparticles (Ag:Cu NPs)

For the synthesis of Ag:Cu NPs, initially, 1.25 g of PVP and 0.5 g of ascorbic acid were taken in a beaker and stirred at 100°C. Additionally, 40 mL of ammonium hydroxide was taken separately in two beakers. In one beaker, 1.7 g of $CuCl_2$ was added, and in the other beaker, 1.7 g of $Ag(NO_3)$ was added. Then both solutions were mixed thoroughly and separately. After obtaining uniform solutions, both solutions were then transferred to the initial solution containing PVP and ascorbic acid, along with the addition of 0.5 g $NaBH_4$,and then maintained with stirring at the same temperature of 100°C for another 4 h. Afterwards, the obtained solution was centrifuged 3–4 times at 7000 rpm for 20 min each to remove the residual product. The obtained sediments were then oven-dried at 60°C to yield the desired grayish silver-colored Ag:Cu NPs.

Synthesis of Ag:Cu/BNSs Nanocomposites

The bimetallic (Ag:Cu)-doped BNS nanocomposites were synthesized using a hydrothermal technique. Here, a fixed amount of 100 mg of as-prepared BNSs was added to three different beakers containing 30 ml of DI water. Subsequently, Ag:Cu NPs with varying mass ratios of 5 wt.%, 10 wt.%, and 15 wt.% were added separately in these beakers and maintained with stirring for 1 h. Afterwards, the mixtures were transferred to a Teflon-lined autoclave for the hydrothermal treatment at 200°C for 12 h. Finally, the obtained products were oven-dried at 80°C to obtain the Ag:Cu-doped BNSs with different weight ratios of 5 wt.%, 10 wt.%, and 15 wt% which were labeled as BCA 5, BCA 10, and BCA 15, respectively.

Electrode Preparation and Electrochemical Measurements

The electrochemical measurements were conducted using a conventional three-electrode cell system in an alkaline medium (1 M KOH) at room temperature with an electrochemical workstation. The working electrode was prepared by patterning the fluorine-doped tin oxide (FTO), which was then coated with the as-prepared electrocatalyst (at 0.5×0.5 cm^2 area). A platinum (Pt) wire was employed as the counter electrode, and Ag/AgCl was used as the reference electrode and immersed in 3 M KCl.

For the electrode preparation, the catalyst ink was prepared using 15 mg of catalyst, 12 µL of Nafion solution as a binder, and 20 µL of ethanol. This solution was ultrasonically mixed for 15 min to obtain a uniform slurry. Subsequently, 10 µL of the as prepared catalyst ink was drop-cast onto a pre-cleaned FTO substrate (using soap solution, DI, acetone, methanol, and IPA followed by UV irradiation) and allowed to dry in air for 2 h. All potentials, measured against the Ag/AgCl electrode, were converted to potential vs. reversible hydrogen electrode using a specific equation.[27,28]

$$E_{\mathrm{RHE}} = E_{\mathrm{Ag/AgCl}} + 0.197 + 0.059\,\mathrm{pH}$$

where E_{RHE} is the potential applied vs. RHE, $E_{\mathrm{Ag/AgCl}}$ is the potential measured with respect to the reference electrode, and pH refers to the electrolyte.

Electrocatalytic performance was determined through linear sweep voltammetry (LSV) at a scan rate of 10 mV s^{-1} and electrochemical surface area (ECSA) was evaluated using cyclic voltammetry (CV). Electrochemical impedance spectroscopy (EIS) studies, ranging from 0.1 KHz to 100 KHz, were conducted to determine the charge transfer resistance of the samples. To assess durability and long-term stability in 1 M KOH, chronoamperometric stability tests were performed for the HER.

Characterization Techniques

The structural behavior of the samples was analyzed by x-ray diffraction (XRD) utilizing Cu Kα-line ($\lambda = 1.54$ Å) on an X'Pert PRO diffractometer. Fourier transform infrared spectroscopy (FTIR) was performed using a Shimadzu IR-Tracer 100H to study the structural chemistry of all the samples. The morphology of the samples was examined by field emission scanning electron microscopy (FESEM, Carl Zeiss Supra 55). The elemental composition and electronic states of the atoms were analyzed using x-ray photoelectron spectroscopy (XPS, Scienta Omicron instrument). To study the charge transfer kinetics, the corresponding LSV, CV, EIS, and long-term stability tests were conducted by chronoamperometry. These tests were performed using an Autolab workstation potentiostat/galvanostat (PGSTAT302).

Results and Discussion

In order to examine the structural properties of BNS and their composites, XRD measurements were conducted as shown in Fig. 1a. The XRD spectra of pristine BNSs show sharp peaks situated at 9.90°, 11.32°, 17.41°, 18.43°, 19.04°, 20.86°, 31.42°, 32.44°, 35.69°, 37.51°, 38.53°, 51.93°, and 59.64° corresponding to (003), (012), (110), (104), (021), (202), (125), (220), (208), (134), (315), (422), and (063) crystal planes. These peaks are characteristic of the β_{12}-rhombohedral crystalline phase of the BNS structure (PDF #89-2777) in space group R-3m with unit cell parameters of $a = b = c = 5.05$ Å and $\alpha = \beta = \gamma = 58.04°$.[29] Upon bimetallic doping in BCA 5, BCA 10, and BCA 15 samples, in addition to boron peaks, new peaks were observed at 38.14°, 64.39°, and 77.4°, corresponding to (111), (220), and (311) planes of the face-centered cubic (fcc) facet of Ag NPs. In addition, the peaks positioned at 32.6° and 44.2° are indexed to the (110) and (111) crystal planes of the fcc structure of CuO and Cu NPs, indicating the successful synthesis of BNS

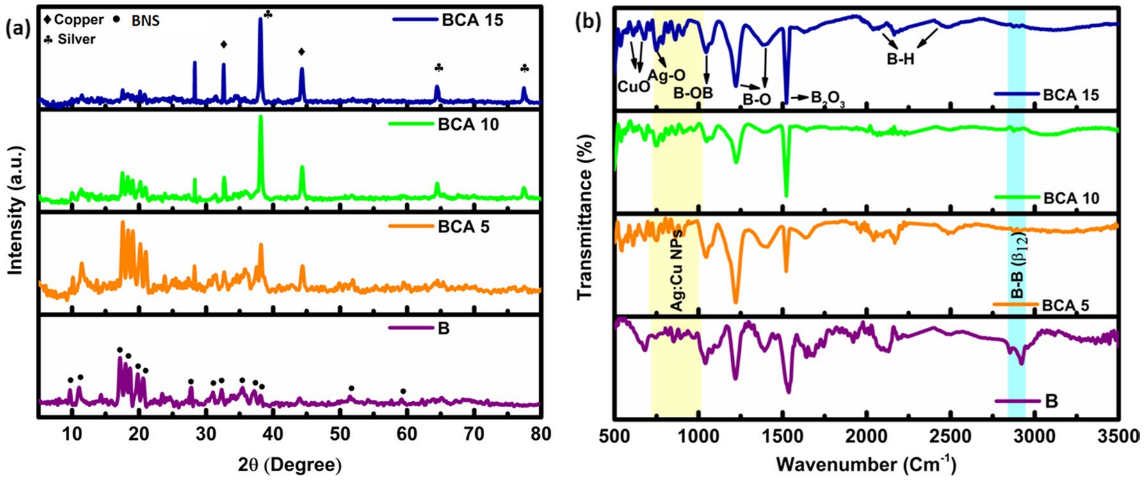

Fig. 1 (a) XRD and (b) FTIR spectroscopy of pristine BNS and its composites BCA5, BCA 10, and BCA 15.

bimetallic composites. Interestingly, both silver and copper NPs show the highest orientation along the (111) plane, which is slightly shifted to a lower angle on increasing the doping concentration, suggesting an increase in lattice constant.[30] In addition, as the bimetallic doping level increases, the BNS structure becomes distorted with a corresponding decrease in the XRD peaks of BNSs. This decrease could be due to an increase in interlayer spacing between the sheets or to the formation of oxygen vacancies.[31] Also, the peak situated at 28.21° is ascribed to the formation of B_2O_3, indicating that the partial oxidation of BNSs increases as the doping concentration increases. Moreover, it has been observed that the diffraction peaks of BNS shift toward lower angles (smaller 2θ values) upon bimetallic doping, which is direct evidence for the increase in the interlayer spacing of BNSs which could be due to intercalation of bimetallic atoms inside the sheets. Thus, the combined effects of both Ag and Cu modulate the boron-layered structure which facilitates complex reaction pathways toward higher catalytic activity.

FTIR spectroscopy was conducted to study the different functional groups present in the materials. As clearly seen from Fig. 1b, pristine BNSs show sharp characteristic bands at 1224 cm^{-1} (B-OB), 1537 cm^{-1} (B-O), 2194 cm^{-1}, and 2489 cm^{-1} (B–H stretching vibrations) which could be due to the sensitive nature of the BNSs on exposure to air. Also, the broad band ranging from 2852 cm^{-1} to 2953 cm^{-1} shows the formation of the β_{12}-rhombohedral phase of BNSs, thus confirming the structural consistency with XRD results. For bimetallic doped nanocomposites, a wide band ranging from 600 cm^{-1} to 900 cm^{-1} is observed, corresponding to the formation of Ag:Cu NPs, which intensifies as the doping level increases. Interestingly, the peaks near 570 cm^{-1}, 621 cm^{-1}, and 675 cm^{-1} correspond to the stretching vibration of CuO. A peak situated at 715.26 cm^{-1} belongs to the Ag-O bending vibrational mode formed due to the partial oxidation of Ag NPs in ambient air.[32] It can be predicted that as the bimetallic doping concentration increases, the peaks of pristine BNSs are suppressed. This phenomenon is beneficial as it provides additional oxygen vacancies to the system. On the other hand, the peak at 1531 cm^{-1} intensifies, which is ascribed to the formation of B_2O_3, suggesting the oxidation of the BNSs at higher doping levels. This oxidation process can hinder the performance of bare materials at higher concentrations.

After the structural analysis, the electronic structure of the BNS and its nanocomposites was analyzed using XPS studies. The core level spectra of B and O for pristine BNS and for Ag, Cu, and B and O for the optimized BCA 10 sample are shown in Fig. 2. The high-resolution spectra of B 1*s* for pristine BNSs is shown in Fig. 2a, which represents the characteristic peaks at 187.85 eV and 188.86 eV indicating two different types of B-B chemical bonds.[14] The broad peak situated at 191.59 eV describes the formation of B_2O_3 due to the partial oxidation of BNSs during their exfoliation process.[33] For the BCA 10 sample, the B1*s* spectra broaden and similar peaks appear as compared to pristine BNSs with a slight shift towards higher binding energies. This might be caused by a modification in the electronic structure of BNSs upon bimetallic doping[34,35] as seen in Fig. 2b.

The high-resolution spectra of Ag 3*d* for the optimized BCA 10 sample are shown in Fig. 2c. It has two major peaks corresponding to Ag-3$d_{5/2}$ and Ag-3$d_{3/2}$with peak-to-peak separation of 6.03 eV, confirming the metallic behavior of Ag nanoparticles.[36] These two peaks were deconvoluted into four sub-peaks in which the peaks situated at 373.63 eV and 367.46 eV show the photoemission of metallic silver (Ag^0) and the peaks located at 374.63 eV and 368.54 eV are attributed to Ag^+ ions owing to the formation of Ag_2O during hydrothermal treatment as predicted in the FTIR results.[37]

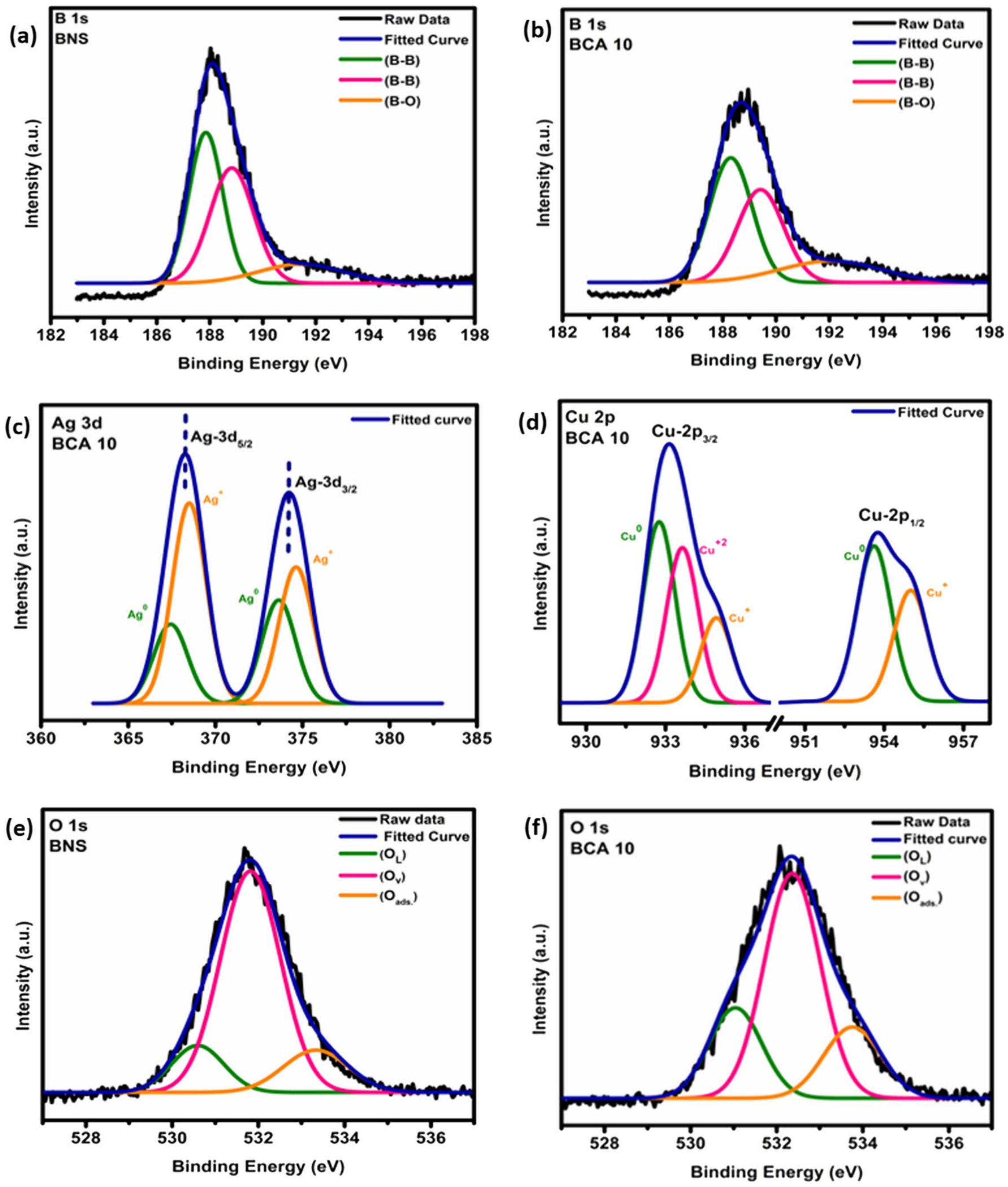

Fig. 2 XPS spectra of B 1*s* for pristine BNS and optimized BCA 10 (a, b); Core level spectra for Ag 3*d* and Cu 2*p* for the BCA 10 sample (c, d) and O 1*s* for pristine BNS and the BCA 10 sample (e, f).

Figure 2d shows the XPS spectra of Cu 2*p* for BCA 10 with two peaks at binding energies of 933.07 eV and 953.77 eV corresponding to Cu-2$p_{3/2}$ and Cu-2$p_{1/2}$. The deconvoluted peaks depict the presence of metallic Cu at 932.76 eV for Cu-2$p_{3/2}$ and 953.62 eV for Cu-2$p_{1/2}$, and the peak located at 933.67 eV in Cu-2$p_{3/2}$ is assigned to the Cu(II) oxidation state resulting from the formation of metal oxide (CuO) as predicted in XRD and FTIR results.[38] The peaks situated at 934.93 eV for Cu-2$p_{3/2}$and 955.04 eV for Cu-2$p_{1/2}$ are ascribed to the presence of Cu^+ ions which could be due to the formation of $Cu(OH)_2$ during the sample's interaction with moisture present in the ambient air.[39]

Additionally, core level spectra of O 1*s* was studied for the pristine BNS and optimized BCA 10 sample as shown in Fig. 2e and f. The peaks situated at 530.56 eV, 531.83 eV, and 533.43 eV correspond to the lattice oxygen (O_L), oxygen vacancy (O_v), and surface water adsorption (O_{ads}), respectively. It has been found that as the bimetallic doping increases in the BCA 10 sample, the O 1*s* spectra broadens and shifts towards higher binding energies which could be due to the formation of oxygen vacancies.[40] Interestingly, the O_v/O_L ratio is an important factor in determining the presence and role of oxygen vacancies and can be predicted from XPS peak area analysis. Accordingly, the corresponding ratio of O_v/O_L was calculated for pristine BNS and optimized BCA 10 samples. Comparatively, the BCA 10 sample shows a higher O_v/O_L ratio of 2.20 than that of the pristine sample, at 1.28. This is attributed to the large number of oxygen vacancies present in the BCA 10 sample which serve as active sites for the adsorption and desorption of reactants and intermediates on the catalyst surface.[41] This increased adsorption capability contributes to improved reaction kinetics, enhancing the catalytic activity and overall performance.

The morphology of the samples was examined using FESEM analysis. Figure 3a shows the clear formation of a layered sheet-like structure of as-prepared pristine BNSs. This structure provides a well-exposed and large surface area. Further, with the introduction of bimetallic dopants (Ag:Cu NPs) in BCA 5, very few quasi-spherical nanoparticles of the bimetallic dopants with average size ranging from 50 nm to 80 nm appeared on the surface of the BNSs, as shown in Fig. 3b.[42] Upon increasing the bimetallic dopant concentration in BCA 10, the dopants almost cover the BNSs, leading to the surface structure modification as displayed in Fig. 3c. From this observation, with a further increase in the concentration in BCA 15, the bimetallic nanoparticles start to agglomerate on the surface of the BNSs. This process leads to oxidation of the BNSs, resulting in the decreased interlayer spacing due to restacking of sheets as evident from Fig. 3d. This phenomenon affects the overall performance of the material. However, it can be observed that despite the oxidation, the layered morphology of the BNSs remains intact even at high doping levels.

The electrochemical performance of the BNS and its composites was analyzed using a three-electrode setup in 1 M KOH for conducting the HER. Initially, linear sweep voltammetry measurement was conducted at a scan rate of 10 mV s^{-1} as shown in Fig. 4a. Of all the samples, the BCA 10 composite shows the most efficient performance with the lowest overpotential value of 0.101 V to achieve current density of 10 mV cm^{-2}. Further, the overpotential values for an optimized sample (BCA 10) were calculated at higher current densities (inset, Fig. 4a) and were found to be 0.102 V, 0.127 V, 0.139 V, and 0.160 V at current density of 10 mA cm^{-2}, 30 mA cm^{-2}, 50 mA cm^{-2}, and 100 mA cm^{-2}, respectively, as shown in the inset of

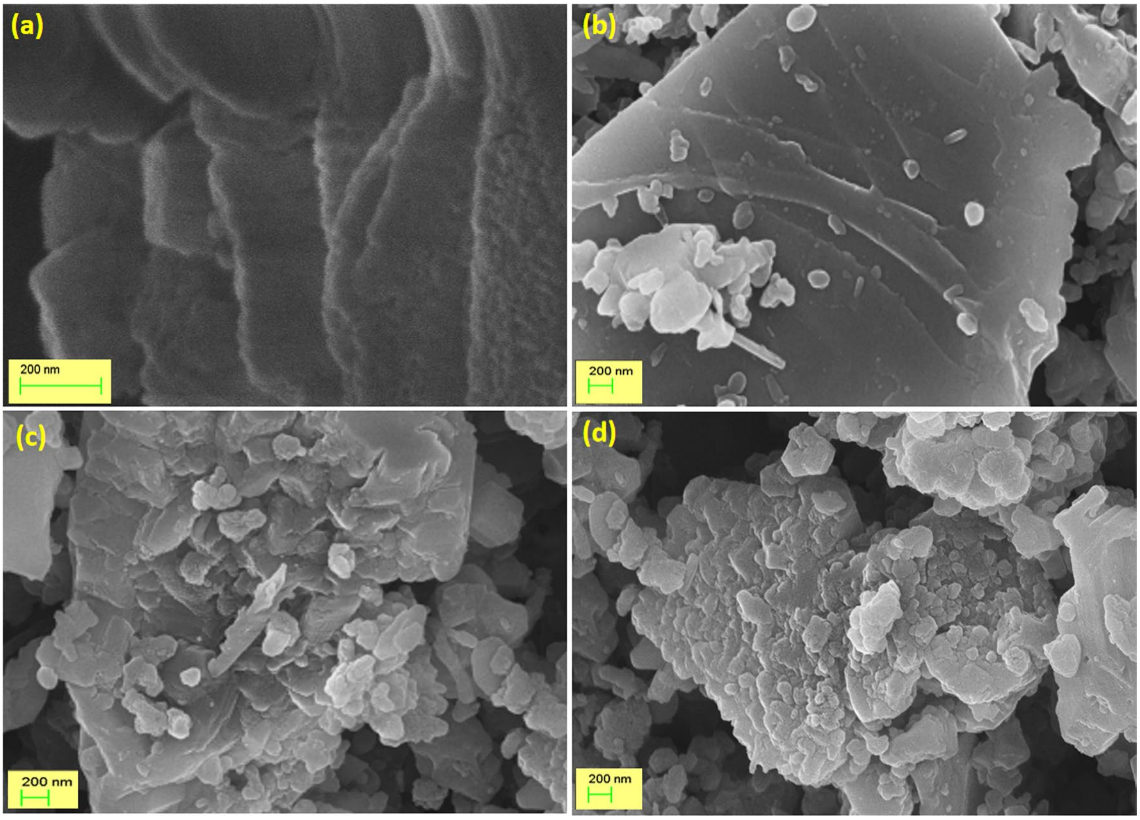

Fig. 3 FESEM images of pristine BNS (a) and its composites BCA 5 (b), BCA 10 (c), and BCA 15 (d).

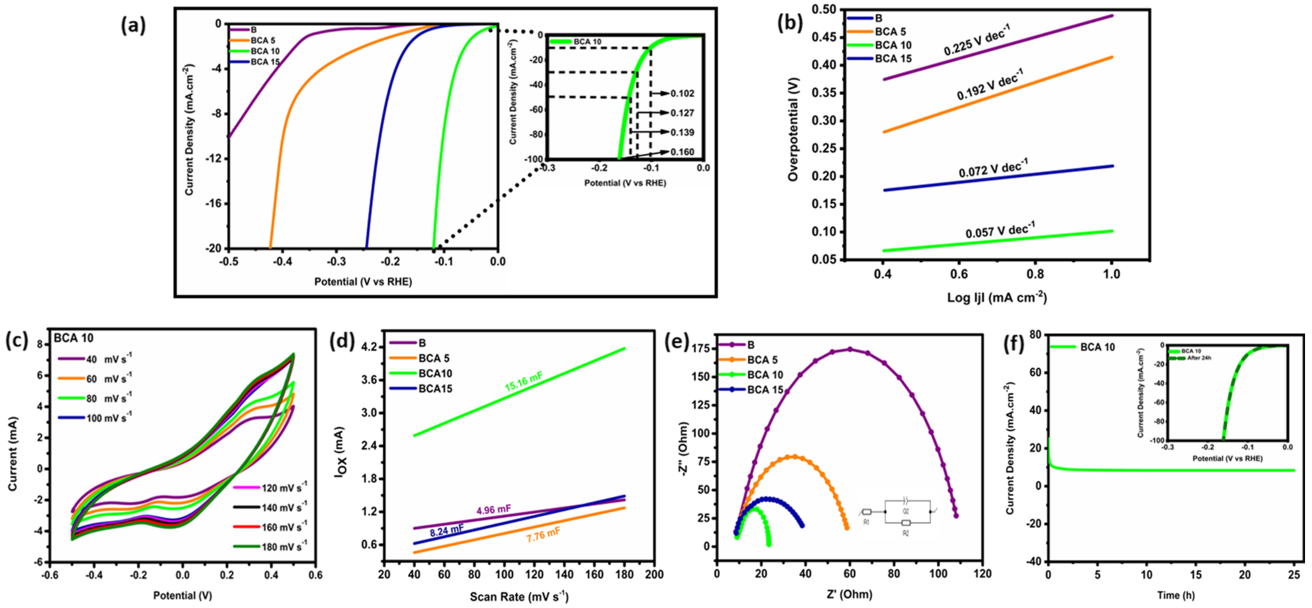

Fig. 4 (a) LSV curve for pristine BNS and its composites, BCA 5, BCA 10, and BCA 15, at 10 mV s^{-1}; inset: Overpotential values for BCA 10 at higher current densities of 10 mA cm^{-2}, 30 mA cm^{-2}, 50 mA cm^{-2}, and 100 mA cm^{-2}, respectively; (b) corresponding Tafel slope for all the samples; (c) CV curve for the optimized BCA 10 sample; (d) double layer capacitance (Cdl) values for all the samples; (e) EIS curve and Nyquist plot for all the samples; inset: the equivalent circuit and (f) chronoamperometry for the BCA 10 sample; inset: LSV curve retention before and after 24 h.

Table I The evaluated parameters of the pristine BNS and its composites BCA 5, BCA 10, and BCA 15 as electrocatalysts for HER

Electrocatalyst	η (V)	Tafel slope (V dec^{-1})	C_{dl} (mF)	ECSA (cm^2)	R_{ct} (Ω)	J_{ex} (mA cm^{-2})	RF	N (10^{-8} Mol)	V_H (μL)
BNS	0.498	0.225	4.96	82.66	102.3	4.12	1180.85	5.14	0.12
BCA 5	0.398	0.192	7.76	129.33	53.4	5.83	1847.57	8.04	0.19
BCA 10	**0.101**	**0.054**	**15.16**	**252.66**	**15.9**	**7.86**	**3609.42**	**15.16**	**0.38**
BCA 15	0.22	0.072	8.24	137.33	38.12	6.10	1961.85	8.54	0.21

Bold values indicate the optimized sample with obtained optimized HER parameters

Fig. 4a. This is due to the synergistic effects of optimal bimetallic doping which promotes the creation of oxygen vacancies that facilitate the charge transfer process by providing a conductive pathway to the charge carriers. This improved charge transfer contributes to efficient electron transfer during electrochemical reactions, leading to enhanced catalytic performance. Moreover, the corresponding Tafel slopes were also calculated from the LSV curves to study the reaction kinetics and the efficiency of hydrogen evolution. Figure 4b reveals that the BCA 10 sample shows a comparatively low Tafel slope value of 0.057 V dec^{-1} suggesting superior catalytic activity and a faster reaction rate for the hydrogen evolution. The highest exchange current density (J_{ex}) was also calculated by extrapolating the Tafel slope to zero overpotential value. The BCA 10 electrocatalyst consistently shows the highest exchange current density of 7.86 mA cm^{-2} indicating the fastest charge transfer kinetics of the carriers. The double layer capacitance (Cdl) was also evaluated by conducting CV measurement at different scan rates (Fig. 4c), to study the interfacial phenomenon between the electrode and electrolyte as shown in Fig. 4d. Here also, BCA 10 shows the highest capacitance of 15.16 mF with the highest electrochemically active surface area (ECSA) of 252.66 cm^2, reflecting the high degree of interaction between the electrocatalyst surface and the electrolyte. This phenomenon is beneficial for the adsorption of reactant species and their subsequent reduction to evolve hydrogen. The overall HER parameters for comparison of all the samples are tabulated in Table I. Consistent with the above measurements, the optimized composite shows the highest number of active HER sites of about 15.16×10^{-8}, which was further verified by analyzing the roughness factor (3609.42) which was also the highest. In addition, the volume of hydrogen evolved was also greatest, at 0.38 μL, for the BCA 10 electrocatalyst. To study the charge transfer mechanism, EIS was conducted to study the electrochemical interfaces involved in HER. The corresponding Nyquist plot along with its equivalent circuit was plotted which shows the smallest semicircle regime for the BCA 10 electrocatalyst as shown in Fig. 4e, depicting the swift charge transfer mechanism between the electrode and electrolyte with a minimum charge transfer resistance R_{ct} of 15.9 Ω. To determine the real-time information regarding the kinetics, activity, and stability of the optimized BCA 10 electrocatalyst, chronoamperometry was conducted over 24 h (Fig. 4f). The optimized electrocatalyst shows excellent long-term stability of the electrode in alkaline medium, making it useful in potential applications. A slight degradation in the LSV curve was observed after this time period which could be due to harsh environmental conditions, highlighting the good retention stability of the BCA 10 electrocatalyst, as shown in the inset of Fig. 4f. Thus, the optimal bimetallic doping in BCA 10 exhibits enhanced resistance to contaminants or by-products present in the environment and helps to maintain catalytic activity over extended periods of time.

Conclusion

In conclusion, the successful fabrication of boron layered structures was achieved by controlled anchoring of bimetallic Ag:Cu nanoparticles with varying concentrations using hydrothermal treatment, and was investigated using HER in alkaline medium. The introduction of bimetallic dopants helped in providing oxygen vacancies within the system upon increasing the concentration from BCA 5 to BCA 10. Further increasing the dopant concentration in the BCA 15 sample resulted in particle agglomeration on the BNS surface, hindering the charge transfer kinetics and thus impeding catalytic activity. Of all the samples, BCA 10 showed remarkable electrocatalytic activity with the lowest overpotential value of 0.101 V at 10 mA cm^{-2}, Tafel slope of 0.057 V dec^{-1}, and lowest interfacial charge transfer resistance of 15.9 Ω for HER. Thus, the combination of the unique properties of BNS with the catalytic activity of Ag and Cu results in synergistic effects useful for enhancing the electrocatalytic performance for the HER.

Acknowledgments The author is thankful to DST-INSPIRE, New Delhi (Award No. IF220162) for providing financial assistance.

Author Contributions Akshidha: Data curation, Formal analysis, Investigation, Methodology, Writing—original draft. Rajnish Dhiman: Data acquisition and supervision. Aman Mahajan: Conceptualization, Project administration, Supervision, Visualization, Methodology, Writing—review and editing.

Data availability Data will be made available on request.

Conflict of interest The authors declare that they have no conflict of interest.

References

1. P.A. Le, V.D. Trung, P.L. Nguyen, T.V. Bac Phung, J. Natsuki, and T. Natsuki, The current status of hydrogen energy: an overview. *RSC Adv.* 13, 28262 (2023).
2. I. Marouani, T. Guesmi, B.M. Alshammari, K. Alqunun, A. Alzamil, M. Alturki, and H. Hadj Abdallah, Integration of renewable-energy-based green hydrogen into the energy future. *Processes* 11, 2685 (2023).
3. S. Wang, A. Lu, and C.-J. Zhong, Hydrogen production from water electrolysis: role of catalysts. *Nano Converg.* 8, 4 (2021).
4. C. Flavio, A. Christian Gonçalves, M. Tatiana Duque, L. Roberto Batista de, R. Antonio Carlos Chaves, C. Leandro de Lima, S. André Mychell Barbieux Silva, M. Monah Marques, C. José William Diniz, S. Geovany Albino de, A. Lucas Fernandes, C. Diericon de Sousa, C. Adão Marcos Ferreira, R. Thiago Soares Silva, G. Pedro Henrique Machado, S. Guilherme Botelho Meireles de, Production of Hydrogen and their Use in Proton Exchange Membrane Fuel Cells, in: E. Murat (Ed.). Advances In Hydrogen Generation Technologies, IntechOpen, Rijeka, **Ch. 4** 63 (2018).
5. Q. Hassan, S. Algburi, A.Z. Sameen, H.M. Salman, and M. Jaszczur, Green hydrogen: a pathway to a sustainable energy future. *Int. J. Hydrog. Energy* 50, 310 (2024).
6. Y. Tang, F. Liu, W. Liu, S. Mo, X. Li, D. Yang, Y. Liu, and S.-J. Bao, Multifunctional carbon-armored Ni electrocatalyst for hydrogen evolution under high current density in alkaline electrolyte solution. *Appl. Catal. B Environ.* 321, 122081 (2023).
7. A. Younis, S. Sehar, X. Guan, S. Aftab, H. Manaa, T. Mahmood, J. Iqbal, F. Akram, N. Ali, and T. Wu, Four-in-one strategy to boost the performance of 3-dimensional MoS_2 nanostructures for industrial effluent treatment and hydrogen evolution reactions. *J. Alloys Compd.* 976, 173104 (2024).
8. Y.-N. Zhou, X. Liu, C.-J. Yu, B. Dong, G.-Q. Han, H.-J. Liu, R.-Q. Lv, B. Liu, and Y.-M. Chai, Boosting hydrogen evolution through hydrogen spillover promoted by Co-based support effect. *J. Mater. Chem. A.* 11, 6945 (2023).
9. J. Wu, J. Su, T. Wu, L. Huang, Q. Li, Y. Luo, H. Jin, J. Zhou, T. Zhai, D. Wang, Y. Gogotsi, and Y. Li, Scalable synthesis of 2D Mo_2C and thickness-dependent hydrogen evolution on its basal plane and edges. *Adv. Mater.* 35, 2209954 (2023).
10. Navjyoti, V. Sharma, V. Bhullar, V. Saxena, A.K. Debnath, and A. Mahajan, Modulation of surface Ti–O species in 2D-$Ti_3C_2T_X$ MXene for developing a highly efficient electrocatalyst for hydrogen evolution and methanol oxidation reactions. *Langmuir* 39, 2995 (2023).
11. A. Liu, X. Liang, X. Ren, W. Guan, M. Gao, Y. Yang, Q. Yang, L. Gao, Y. Li, and T. Ma, Recent progress in mxene-based materials: potential high-performance electrocatalysts. *Adv. Funct. Mater.* 30, 2003437 (2020).
12. R. Yang, and M. Sun, Electronic structures and optical properties of monolayer borophenes. *Spectrochim. Acta A Mol. Biomol. Spectrosc.* 272, 121014 (2022).
13. Y.V. Kaneti, D.P. Benu, X. Xu, B. Yuliarto, Y. Yamauchi, and D. Golberg, Borophene: two-dimensional boron monolayer:

synthesis, properties, and potential applications. *Chem. Rev.* 122, 1000 (2022).

14. G. Tai, M. Xu, C. Hou, R. Liu, X. Liang, and Z. Wu, Borophene nanosheets as high-efficiency catalysts for the hydrogen evolution reaction. *ACS Appl. Mater. Interfaces* 13, 60987 (2021).
15. J.C. Alvarez-Quiceno, R.H. Miwa, G.M. Dalpian, and A. Fazzio, Oxidation of free-standing and supported borophene. *2D Mater.* 4, 025025 (2017).
16. C. Zhang, Z. Zhang, W. Yan, and X. Qin, Effect of doping on the photoelectric properties of borophene. *Adv. Condens. Matter. Phys.* 2021, 3718040 (2021).
17. E. Jelmy, N. Thomas, D. Mathew, J. Louis, N.T. Padmanabhan, V. Kumaravel, H. Hohn, and S. Pillai, Impact of structure, doping and defect-engineering in 2D materials on CO_2 capture and conversion. *React. Chem. Eng.* 6, 1701 (2021).
18. K. Khan, A.K. Tareen, M. Aslam, A. Mahmood, Q. Khan, Y. Zhang, Z. Ouyang, and Z. Guo, Going green with batteries and supercapacitor: two dimensional materials and their nanocomposites based energy storage applications. *Prog. Solid State Chem.* 58, 100254 (2019).
19. L. Lin, Y. Sun, K. Xie, P. Shi, X. Yang, and D. Wang, First-principles study on the catalytic performance of transition metal atom-doped $CrSe_2$ for the oxygen reduction reaction. *Phys. Chem. Chem. Phys.* 25, 15441 (2023).
20. B. Liu, Z. Chen, R. Xiong, X. Yang, Y. Zhang, T. Xie, C. Wen, and B. Sa, Enhancing hydrogen evolution reaction performance of transition metal doped two-dimensional electride Ca_2N. *Chin. Chem. Lett.* 34, 107643 (2023).
21. B.M. Gibbons, M. Wette, M.B. Stevens, R.C. Davis, S. Siahrostami, M. Kreider, A. Mehta, D.C. Higgins, B.M. Clemens, and T.F. Jaramillo, In situ X-ray absorption spectroscopy disentangles the roles of copper and silver in a bimetallic catalyst for the oxygen reduction reaction. *Chem. Mater.* 32, 1819 (2020).
22. A. Ashok, A. Kumar, M.A. Matin, and F. Tarlochan, Probing the effect of combustion controlled surface alloying in silver and copper towards ORR and OER in alkaline medium. *J. Electroanal. Chem.* 844, 66 (2019).
23. Y. Zhu, A. Marianov, H. Xu, C. Lang, and Y. Jiang, Bimetallic Ag–Cu supported on graphitic carbon nitride nanotubes for improved visible-light photocatalytic hydrogen production. *ACS Appl. Mater. Interfaces* 10, 9468 (2018).
24. K. Bhavani, G. Naresh, B. Srinivas, and A. Venugopal, Plasmonic resonance nature of Ag-Cu/TiO_2 photocatalyst under solar and artificial light: Synthesis, characterization and evaluation of H_2O splitting activity. *Appl. Catal. B: Environ.* 199, 282 (2016).
25. P. Zhang, X. Xu, E. Song, X. Hou, X. Yang, J. Mi, J. Huang, and C. Stampfl, Transition metal-doped α-borophene as potential oxygen and hydrogen evolution electrocatalyst: a density functional theory study. *Catal. Commun.* 144, 106090 (2020).
26. C. Li, X. Liu, D. Wu, H. Xu, and G. Fan, Theoretical study of transition metal doped α-borophene nanosheet as promising electrocatalyst for electrochemical reduction of N_2. *Comput. Theor. Chem.* 1213, 113732 (2022).
27. S. Khan, C. Wang, H. Lu, Y. Cao, Z. Mao, C. Yan, and X. Wang, In-situ tracking of phase conversion reaction induced metal/metal oxides for efficient oxygen evolution. *Sci. China Mater.* 64, 362 (2021).
28. B. Mondal, S. Dinda, N. Karjule, S. Mondal, A. Raja Kottaichamy, M. Volokh, and M. Shalom, The implications of coupling an electron transfer mediated oxidation with a proton coupled electron transfer reduction in hybrid water electrolysis. *ChemSusChem.* 16, e202202271 (2023).
29. C. Ma, P. Yin, K. Khan, A.K. Tareen, R. Huang, J. Du, Y. Zhang, Z. Shi, R. Cao, S. Wei, X. Wang, Y. Ge, Y. Song, and L. Gao, Broadband nonlinear photonics in few-layer borophene. *Small* 17, 2006891 (2021).
30. Y.-H. Chen, P.-I. Lee, S. Sakalley, C.-K. Wen, W.-C. Cheng, H. Sun, and S.-C. Chen, Enhanced electrical properties of copper nitride films deposited via high power impulse magnetron sputtering. *Nanomater.* 12, 2814 (2022).
31. N. Österbacka, and J. Wiktor, Influence of oxygen vacancies on the structure of $BiVO_4$. *J. Phys. Chem. C* 125, 1200 (2021).
32. A.A. Fayyadh, and M.H. Jaduaa Alzubaidy, Green-synthesis of Ag_2O nanoparticles for antimicrobial assays. *J. Mech. Behav. Mater.* 30, 228 (2021).
33. F. Zhang, L. She, C. Jia, X. He, Q. Li, J. Sun, Z. Lei, and Z.-H. Liu, Few-layer and large flake size borophene: preparation with solvothermal-assisted liquid phase exfoliation. *RSC Adv.* 10, 27532 (2020).
34. P.S. Bagus, E.S. Ilton, and C.J. Nelin, The interpretation of XPS spectra: insights into materials properties. *Surf. Sci. Rep.* 68, 273 (2013).
35. J. Gao, J. Cong, Y. Wu, L. Sun, J. Yao, and B. Chen, Bimetallic Hofmann-type metal-organic framework nanoparticles for efficient electrocatalysis of oxygen evolution reaction. *ACS Appl. Energy Mater.* 1, 5140 (2018).
36. P.J. Boruah, P. Kalita, and H. Bailung, Synergistic role of oxygen vacancy defect and plasmonics on modulating the photocatalytic activity of Ag/CuO_x nanocomposites synthesized via solution plasma. *Surf. Interfaces* 43, 103539 (2023).
37. A.K. Mohamedkhair, Q.A. Drmosh, and Z.H. Yamani, Silver nanoparticle-decorated tin oxide thin films: synthesis, characterization, and hydrogen gas sensing. *Front. Mater. Sci.* 6, 188 (2019).
38. Z. Qin, W. Zhang, M. Yu, L. Cui, X. Cao, and J. Liu, Super-light Cu@Ni nanowires/graphene oxide composites for significantly enhanced microwave absorption performance. *Sci. Rep.* 7, 1584 (2017).
39. A. Roy, A. Mukhopadhyay, S. Das, G. Bhattacharjee, A. Majumdar, and R. Hippler, Surface stoichiometry and optical properties of Cu_x–Ti_yC_z thin films deposited by magnetron sputtering. *Coatings* 9, 551 (2019).
40. I. Fongkaew, R. Akrobetu, A. Sehirlioglu, A. Voevodin, S. Limpijumnong, and W.R.L. Lambrecht, Core-level binding energy shifts as a tool to study surface processes on $LaAlO_3$/$SrTiO_3$. *J. Electron Spectrosc. Relat. Phenom.* 218, 21 (2017).
41. C. Wang, Y. Lu, Y. Zhang, H. Fu, S. Sun, F. Li, Z. Duan, Z. Liu, C. Wu, Y. Wang, H. Sun, and Z. Yan, Ru-based catalysts for efficient CO_2 methanation: synergistic catalysis between oxygen vacancies and basic sites. *Nano Res.* 16, 12153 (2023).
42. M. Ikram, S. Abbasi, A. Haider, S. Naz, A. Ul-Hamid, M. Imran, J. Haider, and A. Ghaffar, Bimetallic Ag/Cu incorporated into chemically exfoliated MoS_2 nanosheets to enhance its antibacterial potential: in silico molecular docking studies. *Nanotechnology* 31, 275704 (2020).